Universiteit Antwerpen

This item is the archived peer-reviewed author-version of:

Disruption of self-organized striated structure induced by secondary electron emission in capacitive oxygen discharges

Reference:
Wang Li, Wen De-Qi, Zhang Quan-Zhi, Song Yuan-Hong, Zhang Yu-Ru, Wang You-Nian.- Disruption of self-organized striated structure induced by secondary electron emission in capacitive oxygen discharges
Plasma sources science and technology / Institute of Physics [Londen] - ISSN 0963-0252 - 28:5(2019), 055007
Full text (Publisher's DOI): https://doi.org/10.1088/1361-6595/AB17AE
To cite this reference: https://hdl.handle.net/10067/1603650151162165141

uantwerpen.be
Institutional repository IRUA

Plasma Sources Science and Technology

ACCEPTED MANUSCRIPT

Disruption of self-organized striated structure induced by secondary electron emission in capacitive oxygen discharges

To cite this article before publication: Li Wang *et al* 2019 *Plasma Sources Sci. Technol.* in press https://doi.org/10.1088/1361-6595/ab17ae

Manuscript version: Accepted Manuscript

Accepted Manuscript is "the version of the article accepted for publication including all changes made as a result of the peer review process, and which may also include the addition to the article by IOP Publishing of a header, an article ID, a cover sheet and/or an 'Accepted Manuscript' watermark, but excluding any other editing, typesetting or other changes made by IOP Publishing and/or its licensors"

This Accepted Manuscript is **© 2018 IOP Publishing Ltd**.

During the embargo period (the 12 month period from the publication of the Version of Record of this article), the Accepted Manuscript is fully protected by copyright and cannot be reused or reposted elsewhere.
As the Version of Record of this article is going to be / has been published on a subscription basis, this Accepted Manuscript is available for reuse under a CC BY-NC-ND 3.0 licence after the 12 month embargo period.

After the embargo period, everyone is permitted to use copy and redistribute this article for non-commercial purposes only, provided that they adhere to all the terms of the licence https://creativecommons.org/licences/by-nc-nd/3.0

Although reasonable endeavours have been taken to obtain all necessary permissions from third parties to include their copyrighted content within this article, their full citation and copyright line may not be present in this Accepted Manuscript version. Before using any content from this article, please refer to the Version of Record on IOPscience once published for full citation and copyright details, as permissions will likely be required. All third party content is fully copyright protected, unless specifically stated otherwise in the figure caption in the Version of Record.

View the article online for updates and enhancements.

This content was downloaded from IP address 129.175.97.14 on 13/04/2019 at 04:53

Disruption of self-organized striated structure induced by secondary electron emission in capacitive oxygen discharges

Li Wang[1], De-Qi Wen[2], Quan-Zhi Zhang[3], Yuan-Hong Song[1]*, Yu-Ru Zhang[1] and You-Nian Wang[1]

[1]*Key Laboratory of Materials Modification by Laser, Ion, and Electron Beams (Ministry of Education), School of Physics, Dalian University of Technology, Dalian 116024, People's Republic of China*

[2]*Department of Electrical and Computer Engineering, Michigan State University, East Lansing, MI 48824, United. States*

[3]*Research Group PLASMANT, University of Antwerp, Universiteitsplein 1, B-2610 Antwerp-Wilrijk, Belgium*

[*]*E-Mail: songyh@dlut.edu.cn*

Accepted Manuscript

Abstract

Self-organized striated structure has been observed experimentally and numerically in CF_4 plasmas in radio-frequency capacitively coupled plasmas (RF CCPs) recently (Liu et al 2016 *Phys. Rev. Lett.* **116** 255002). In this work, the striated structure is investigated in a capacitively coupled oxygen discharge with the introduction of the effect from the secondary electron emission, based on a particle-in-cell/Monte Carlo collision model (PIC/MCC). As we know, the transport of positive and negative ions plays a key role in the formation of striations in electronegative gases, for which, the electronegativity needs to be large enough. As the secondary electron emission increases, electrons in the sheaths gradually contribute more ionization to the discharge. Meanwhile, the increase of the electron density, especially in the plasma bulk, leads to an increased electrical conductivity and a reduced bulk electric field, which would shield the ions' mobility. These changes result in enlarged striation gaps. And then, with more emitted electrons, obvious disruption of the striations is observed accompanied with a transition of electron heating mode. Due to the weakened field, the impact ionization in the plasma bulk is attenuated, compared with the enhanced ionization caused by secondary electrons. This would lead to the electron heating mode transition from striated (STR) mode to γ-mode. Besides, our investigation further reveals that γ-mode is more likely to dominate the discharge under high gas pressures or driving voltages.

Keywords: capacitively coupled oxygen plasma, secondary electron emission, striations, electron heating mode transition

Accepted Manuscript

1. INTRODUCTION

Radio-frequency capacitively coupled plasmas (RF CCPs) are widely used in many high-tech applications, such as plasma etching or plasma enhanced chemical vapor deposition (PECVD) in semiconductor manufacturing [1–3]. In practical plasma processing, different properties [4–7] are usually noticed in strongly electronegative discharges characterized by a relatively large ratio between negative ion and electron density: $\eta = n_-/n_e$, which is different from electropositive or weakly electronegative discharges [8–10]. Among these properties, the most fundamental one is the low electrical conductivity and large ion inertia-induced relatively high drift electric field in the bulk region, where positive and negative particles are the main species of charged particles. Besides the drift field inside the plasma bulk, ambipolar fields near the sheath edges also appear. Electrons could be accelerated by the drift-ambipolar (DA) field and then sustain the discharge through ionization collision with neutrals, i.e. DA mode [11–13]. Unlike α-mode [14–17] and γ-mode [18, 19], which mainly arise near the sheath edges caused by sheath expansion and in the sheaths caused by secondary electrons, the DA mode mainly occurs in the plasma bulk or near the sheath edges. Moreover, besides the DA mode, Liu et al. proposed a new electron heating mode in electronegative gas recently, i.e. STR mode [20–22]. They found that the electric field in the plasma bulk is striated and electrons are accelerated within these striated fields when some certain conditions are met in CF_4 gas discharges.

Indeed, lots of related numerical [23, 24] and experimental [25, 26] studies have been focused on the electron heating mechanisms in both electronegative or electropositive CCPs, for which, the discharge modes and mode transitions [27–29] dependent on different external parameters are always studied as the important considerations. Generally, at low pressures or voltages, the discharge is always sustained in α-mode and would transfer to be in γ-mode with increasing pressure and voltage. DA mode [30, 31] largely depends on the electronegativity, and the STR mode would appear only when the driving frequency is close to the plasma ion frequency [22]. Besides these typical heating modes, the electric field reversal [32, 33], which is usually present during sheath collapse, is also observed in some investigations to make contributions to the electron heating. Godyak et al experimentally demonstrated the transition between α-mode and γ-mode, by observing the evolution of the electron energy distribution function (EEDF) in low pressure argon and helium RF

Accepted Manuscript

discharges [34]. Denpoh et al [35, 36] and Proshina et al [31] studied the transition from DA mode into α-mode by decreasing the pressure and/or increasing the voltage in CF_4 discharges. In study of the self-organized striations in electronegative gas, Liu et al found that the striations would disappear when the driving frequency becomes large, especially larger than the ion plasma frequency, with the transition from STR mode to DA mode [22]. Besides, in their latest research they found that the transition could also appear by adjusting the voltage amplitude, gas pressure or electrode gap [21]. However, in all of the related investigations of STR mode, the effect of secondary electron emission on discharges was not taken into account so far, neither was the transition of the electron heating mode caused by it.

The generation mechanism of the striations in electronegative gases has been explained in previous studies [20–22]and two conditions are necessary: firstly, the electronegativity is high enough; secondly, the RF driving frequency is comparable to the ion plasma frequency. If both the two conditions are simultaneously met, the positive and negative ions would oscillate back and forth in the opposite directions. As a result, the separation of the positive and negative charges induces an "internal" electric field, which would be superimposed on the drift field, leading to a striated total field in the bulk. An analytical ion-ion model was developed in Ref. [22], from which, the ion displacement could be calculated and some physical mechanisms behind could be explained. For simplicity, the motion of positive and negative ions is solved in the so called ion-ion plasma in their model, without considering the effect from electrons. However, in our investigations of oxygen discharges, we find that the introduction of secondary electron effects may become an important factor that impacts the formation of the striation structure.

As known, oxygen plasmas have been widely used in various material processing applications, such as etching of polymer films and improvement of surface properties [37, 38]. However, due to the presence of metastable molecules and atoms, the chemistry in oxygen discharges is complicated. The singlet delta metastable molecule $O_2(a^1\Delta_g)$, in particular, has been demonstrated to play an significant role in the discharge. Both in experiments and simulations, the density of $O_2(a^1\Delta_g)$ has been confirmed to have great influence on the electronegativity for the significant contribution of the associative detachment process $O^- + O_2(a^1\Delta_g) \rightarrow O_3 + e$ to the loss of O^- [39–42]. In order to take the effects of $O_2(a^1\Delta_g)$ into account in the simulations, several methods have been adopted in some investigations.

Accepted Manuscript

Bronold et al assumed a homogeneous spatial density of the $O_2(a^1\Delta_g)$, which is considered to be a fraction of the O_2 density [43]. The determination of the $O_2(a^1\Delta_g)$ content in their simulation is relatively crude but effective in comparison with experiments. Derzsi et al estimated the density of $O_2(a^1\Delta_g)$ from a balance equation, by which, the wall quenching of $O_2(a^1\Delta_g)$ is taken into account and the $O_2(a^1\Delta_g)$ content could be calculated dependent on external parameters [44]. Gudmundsson et al kinetically considered the metastable $O_2(a^1\Delta_g)$ molecule and the metastable $O(^1D)$ atom in their model and demonstrated that, if the metastable molecule $O_2(a^1\Delta_g)$, the metastable atom $O(^1D)$ and the corresponding reactions are included in the simulation, the peak O_2^+ ion density is roughly 30% lower than that if all of the metastable molecule involved reactions are omitted [45]. Therefore, from the studies given above, we can see that the treatment of $O_2(a^1\Delta_g)$ should be carefully considered in the model.

In this work, by performing a PIC/MCC simulation, we examine the secondary electron emission effects on the striated structure and electron heating modes in oxygen CCP discharges. The effects of the driving voltage and discharge pressure on the discharge mechanism are the important considerations. The increase of the striation gap and the final striation disruption are presented as the secondary electron emission becomes strong. It is indicated that, even in strongly electronegative discharges, the behavior of electrons have great influences on the structure of the striations. Besides, the transition from STR mode to γ-mode caused by the secondary electrons is also discussed.

This paper is organized as follows. In section 2, a short description of the PIC/MCC method is given. The simulation results are present in section 3, in which, two parts are involved. In the first part, we discuss the striation structure, and transition of operation modes with the secondary electron emission coefficient over a domain of $0 - 0.21$ and other parameters fixed. In the second part, fixing the emission coefficient, we investigate the influence of the gas pressure and driving voltage on the operation mode transition. Finally, a conclusion is given in section 4.

2. PIC/MCC SIMULATION METHODS

We employ a 1d3v (one-dimensional in space and three-dimensional in velocity) electrostatic Particle-in-Cell method coupled with a Monte Carlo treatment of collision processes.

Accepted Manuscript

TABLE I: List of the collisions considered in oxygen simulations. The references for the cross sections are presented in the last column.

#	Reaction	Process	Reference
1.	$e+O_2 \rightarrow O_2+e$	Elastic scattering	xpdp1[50]
2.	$e+O_2(r=0) \rightarrow O_2+e(r>0)$	Rotational excitation	xpdp1
3.	$e+O_2(v=0) \rightarrow O_2+e(v=1)$	Vibrational excitation	xpdp1
4.	$e+O_2(v=0) \rightarrow O_2+e(v=2)$	Vibrational excitation	xpdp1
5.	$e+O_2(v=0) \rightarrow O_2+e(v=3)$	Vibrational excitation	xpdp1
6.	$e+O_2(v=0) \rightarrow O_2+e(v=4)$	Vibrational excitation	xpdp1
7.	$e+O_2 \rightarrow e+O_2(a^1\Delta_g)$	Metastable excitation (0.98eV)	xpdp1
8.	$e+O_2 \rightarrow e+O_2(b^1\Sigma_g)$	Metastable excitation (1.63eV)	xpdp1
9.	$e+O_2 \rightarrow O^-+O$	Dissociative attachment (4.2eV)	xpdp1
10.	$e+O_2 \rightarrow e+O_2$	Excitation (4.5eV)	xpdp1
11.	$e+O_2 \rightarrow e+O(3P)+O(3P)$	Dissociation (6.0eV)	xpdp1
12.	$e+O_2 \rightarrow e+O(3P)+O(1D)$	Dissociation (8.4eV)	xpdp1
13.	$e+O_2 \rightarrow e+O(1D)+O(1D)$	Dissociation (10.0eV)	xpdp1
14.	$e+O_2 \rightarrow e+O+O(3p^3P)$	Dissociative excitation (14.7eV)	xpdp1
15.	$e+O_2^+ \rightarrow O(3P)+O(1D)$	Dissociative recombination	xpdp1
16.	$e+O_2 \rightarrow e+O_2^++e$	Ionization (12.06eV)	oopd1[51]
17.	$e+O^- \rightarrow O+2e$	Electron-impact detachment	oopd1
18.	$O^-+O_2(a^1\Delta_g) \rightarrow O_3+e$	Associative detachment	[43]
19.	$O^-+O_2 \rightarrow O+O_2+e$	Detachment	oopd1
20.	$O^-+O_2 \rightarrow O^-+O_2$	Scattering	oopd1
21.	$O^-+O_2^+ \rightarrow O+O_2$	Mutual neutralization	oopd1
22.	$O_2^++O_2 \rightarrow O_2+O_2^+$	Charge exchange	oopd1
23.	$O_2^++O_2 \rightarrow O_2^++O_2$	Scattering	oopd1

The discharge is assumed to be operated between two 25 cm radius electrodes separated by a gap of $L = 3$ cm. One electrode at $x = 0$ is driven by a cosine voltage source and the other at $x = L$ is grounded.

Three main charged species are traced in the PIC model: O^-, O_2^+ and e^-. As known, the

Accepted Manuscript

complicated collision processes in oxygen discharges are essential to be dealt with, especially the collisions involving the generation and loss of O^-, such as the associative detachment process between O^- and $O_2(a^1\Delta_g)$. The cross sections or reaction rates of these collisions affect the electronegativity as the discharge reaches steady state, and would further determine the operation mechanism and plasma properties. Therefore, it is necessary to figure out a set of reliable cross sections for these collisions and methods to calculate the content of metastable state in the chamber. In order to obtain more accurate simulation results, several ways of handling these collision processes in oxygen discharge have been discussed in some previous researches [46–49]. For example, in the oopd1 code put forward in [51], the oxygen atom in the ground state $O(^3P)$, ion of the oxygen atom O^+, the relevant reactions as well as some revised cross sections from the well established xpdp1 [50] code are taken into account besides O_2, O_2^+, O^-, and e^-. As a subsequent study, the singlet metastable molecule $O_2(a^1\Delta_g)$ and the metastable oxygen atom $O(^1D)$ have been added to the reaction set since their significant influence on the discharge [45].

Previous studies have indicated that the density of $O_2(a^1\Delta_g)$ may depend on its wall quenching coefficient, which is greatly determined by the surface material, the surface temperature and roughness [52–55]. When the wall quenching coefficient is set to be 1×10^{-5}, the simulation results agree well with the experimental observation for the stainless steel electrode in Greb A et al's work [39], corresponding to an $O_2(a^1\Delta_g)$ content of 15% and a time and space averaged electronegativity of 1.2. While for Teflon electrode, the best matching result is obtained by adopting a quenching coefficient of 3×10^{-3}, with an $O_2(a^1\Delta_g)$ content less than 1% and a higher electronegativity of 12.5. Moreover, they also demonstrated that the increased wall quenching coefficient leads to decreased $O_2(a^1\Delta_g)$ content, which further results in increased electronegativity. This is consistent with the observations in Derzsi et al [44] and Proto et al's work [52]. Derzsi et al obtained good comparisons with the experiment when quenching coefficient of 6×10^{-3} is fixed in their PIC/MCC model. A higher and larger scope of time and space averaged electronegativity from 0 to 60 was found under this quenching coefficient and their discharge parameters [56]. Proto et al listed the $O_2(a^1\Delta_g)$ wall quenching coefficient for different surface materials at room temperature, and explored the influence of the $O_2(a^1\Delta_g)$ quenching coefficient on the electron heating mechanism and the electron energy probability function in detail [52].

The collision processes adopted in our simulations mainly follow the work of Derzsi et al

Accepted Manuscript

[44, 56, 57], which has been validated by several experiments. Most of the collision cross sections refer to the xpdp1 [50] and oopd1 [51] procedure, except the associative detachment process (reaction 18 in table 1), which refers to [43]. The collision processes taken into account in our model and the references of the cross sections are listed in table 1. For the content of the singlet metastable molecule $O_2(a^1\Delta_g)$, a homogeneous spatial density is assumed, and the density is estimated from a balance equation, as did in Derzsi's work [44], i.e., the electron impact excitation of O_2 (process 7) is considered to be the source of $O_2(a^1\Delta_g)$, and the molecules are assumed to predominantly lost by quenching at the electrodes. In our simulations, the $O_2(a^1\Delta_g)$ wall quenching coefficient is set as a fixed value of 6×10^{-3}, which is also consistent with their work and has been confirmed to be reasonable by the experiments [44, 56].

The particles are explicitly pushed in all the simulations. The space and time step are fixed to 6×10^{-5} m and 1.6×10^{-11} s, respectively. More than 100 particles are considered in one cell and typically 5000 RF cycles are needed for equilibrium. We assume the temperature of oxygen to be 300 K and neglect the electron reflection at the electrodes.

3. SIMULATION RESULTS

3.1 Striation disruption and electron heating mode transition

Figure 1 shows the axial profiles of charged species densities, net charge density and electric field at $t = 0.25\ T_{RF}$ and $t = 0.75\ T_{RF}$ under different secondary electron emission coefficients, with the driving frequency $f = 6$ MHz, voltage amplitude $V = 200$ V, and gas pressure $P = 40$ Pa. In order to be better observed, the electron density has been enlarged by a factor of 10 when the secondary electron emission coefficient γ_{se} is set to 0.0, 0.15 and 0.18. Similar to the characteristics in CF_4 discharges at low frequencies [20], the ion densities exhibit "comb-like"profiles in this strongly electronegative bulk as shown in figure 1(a1), (a2), (b1), (b2), (c1), and (c2), which indicates the establishment of striation structure. However, it is seen that the gap distance between two neighboring peaks are enlarged and the number of the density peaks decreases with the increasing γ_{se}. We calculated the average striation gap for different γ_{se}, which is 0.12 cm for $\gamma_{se} = 0.0$, 0.16 cm for $\gamma_{se} = 0.15$, and 0.19 cm for $\gamma_{se} = 0.18$. Particularly, no "comb-like"structure could be observed in the ion

Accepted Manuscript

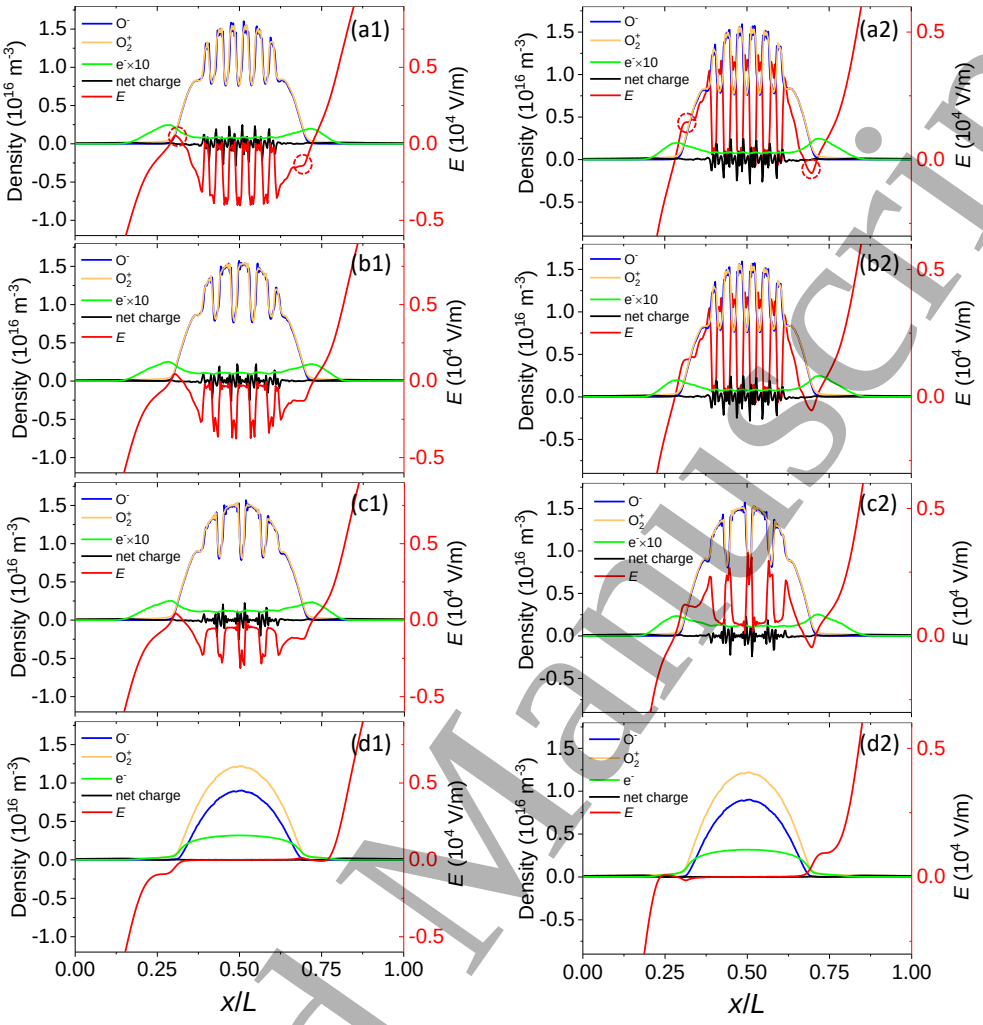

FIG. 1: Axial profiles of charged species densities, net charge density, and electric field at the time $t = 0.25\ T_{\mathrm{RF}}$ (first column) and $t = 0.75\ T_{\mathrm{RF}}$ (second column) at different secondary electron emission coefficients. The electron density is multiplied by a factor of 10 at $\gamma_{\mathrm{se}} = 0.0$, $\gamma_{\mathrm{se}} = 0.15$, and $\gamma_{\mathrm{se}} = 0.18$. The discharge parameters are: driving frequency $f = 6$ MHz, voltage amplitude $V = 200$ V, and gas pressure $P = 40$ Pa.

density profiles in figure1(d1) and (d2) at $\gamma_{\mathrm{se}} = 0.21$, which indicates that the striations are completely disrupted. Thus, the secondary electrons could greatly affect the striation structure, even leads to the disruption of it. In the following, we will discuss the main reasons for the changing of the striation structure, which is greatly related to the electron density and electronegativity.

The transient electric field is shown in each plot of figure 1 with red line. When γ_{se} is

Accepted Manuscript

set to 0.0, 0.15 and 0.18, the total electric field is a superposition of the "internal" field produced by charge separation and the drift field caused by low conductivity in the bulk of RF driven electronegative plasmas, as shown in the first three rows in figure 1. To be more specific, during the first half of the RF period, O_2^+ ions are accelerated to the powered electrode ($x = 0$) and O^- ions are accelerated to the grounded electrode ($x = L$) by the negative drift field inside the bulk region. Therefore, the charge separation is produced (black line) and the internal electric field is set up, which shows positive or negative at the positions of maximum or minimum ion densities. However, due to the negative drift field, the total field is negative with a larger magnitude at the valley locations of the ion densities and is nearly zero or weakly negative near the peaks of the ion densities, resulting in a striated total field, as shown in figure 1(a1), (b1) and (c1). Whereas during the second half of the RF period, the drift field is positive accompanied by a reversed "internal" electric field, leading to a positive total field near the valleys of the ion densities, and a nearly zero but still positive field near the peaks of the ion densities. Thus, the striated electric field reverses periodically. However, no drift field or "internal" field could be generated in the bulk at $\gamma_{\rm se} = 0.21$, leading to the disappearance of the striated field here.

Indeed, at $t = 0.25\ T_{\rm RF}$ and $0.75\ T_{\rm RF}$, for the reason that the negative ions could not effectively respond to the sheath oscillation and are assembled in the bulk region, electron density peaks are observed near the two sheath edges to keep the quasineutrality of the bulk. Then, due to the large gradient on the bulk side of the two peaks, electrons diffuse into the bulk, accompanied by the O_2^+ ions' continuously flow to the electrodes. As a result, besides the striated field in the bulk, ambipolar electric fields also arise near the sheath edges, which are marked out with the dashed red circles in figure 1 (a1) and (a2). Similar ambipolar fields could also be observed at $\gamma_{\rm se} = 0.15$ and 0.18 at the same positions. But at $\gamma_{\rm se} = 0.21$, it is seen that no electron density peaks are formed near the sheath edges in figure 1(d1) and (d2), for which, the electron density is highest near the discharge center.

Figure 2 shows the axial profiles of charged species densities, net charge density and electric field at $t = 0.5\ T_{\rm RF}$ with $\gamma_{\rm se} = 0.0$ (a) and $\gamma_{\rm se} = 0.21$ (b) respectively. As we know, the drift field is small even close to zero at this time, but the internal striated field still exists in figure 2(a) owing to the inertia of the ions, leading the total field to be positive near the peaks of the ion density, which is different from figure 1(a1). Besides, for the reason that the sheath near the powered electrode is fully expanded, there is no electron accumulation

Accepted Manuscript

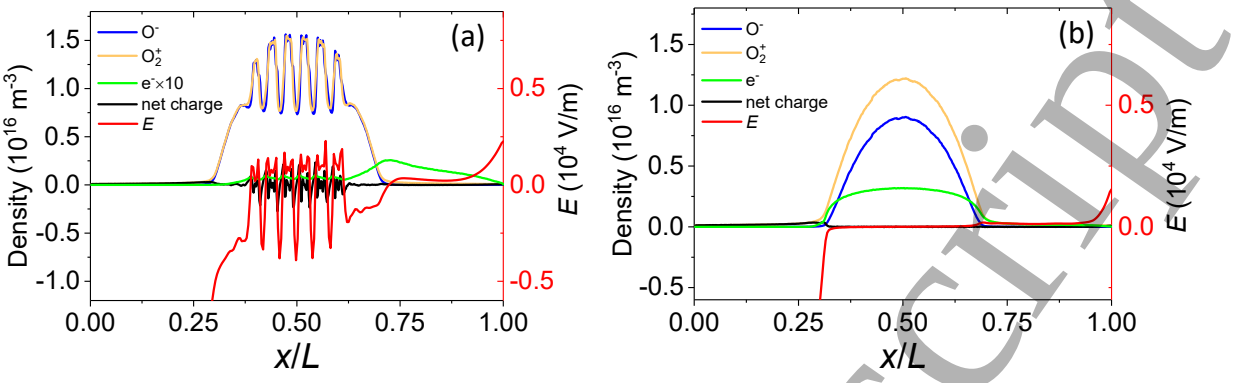

FIG. 2: Axial profiles of charged species densities, net charge density, and electric field at the time $t = 0.5\ T_{\mathrm{RF}}$ with $\gamma_{\mathrm{se}} = 0.0$ (a) and $\gamma_{\mathrm{se}} = 0.21$ (b) respectively. The electron density is multiplied by a factor of 10 at $\gamma_{\mathrm{se}} = 0.0$. The conditions are the same as in figure 1.

here to ensure the quasineutrality. Thus, the electron density only has one peak near the grounded electrode. Correspondingly, the ambipolar electric field also appears only on this side. Therefore, the ambipolar electric field due to the electron accumulation occurs as the sheath collapses and disappears until the sheath approaches to the maximum width. When γ_{se} is set to 0.21, no ambipolar electric field could be observed on both sides of the electrode in figure 2(b).

Figure 3 shows the emission coefficient dependence of spatio-temporal distribution of electron-impact dissociation rate in the first column (i.e. corresponding to reaction 12 ($e + O_2 \rightarrow e + O(3P) + O(1D)$) in table 1), electron-impact ionization rate in the second column, electric field in the third column, net charge density in the fourth column, and electron power absorption rate in the fifth column, separately. The operation conditions are same with those in figure 1. As shown, apparent charge separation is established in the profiles of the net charge density, and striated structures are displayed in the electric field profiles when the emission coefficient of secondary electron is less than 0.18. These results are consistent with those of the net charge density and electric field shown in figure 1. Being accelerated by the striated field, electrons obtain energy in the bulk. The time-dependent electron absorption power rate in the fifth column is calculated by $P_e = J_e \cdot E$, with J_e the electron current density and E the electric field, respectively. Due to almost uniform electron flux in the plasma bulk, the electron absorption power rate is largely modulated by the electric field and also in striated distribution. When the electrons are accelerated to

Accepted Manuscript

the corresponding threshold values, inelastic collisions, such as dissociation and ionization, occur. Remarkably, the ions' production by ionization impacts etc., should compensate for the losses caused by recombination impacts etc., at each peak of the ion density to keep the stability of the striations.

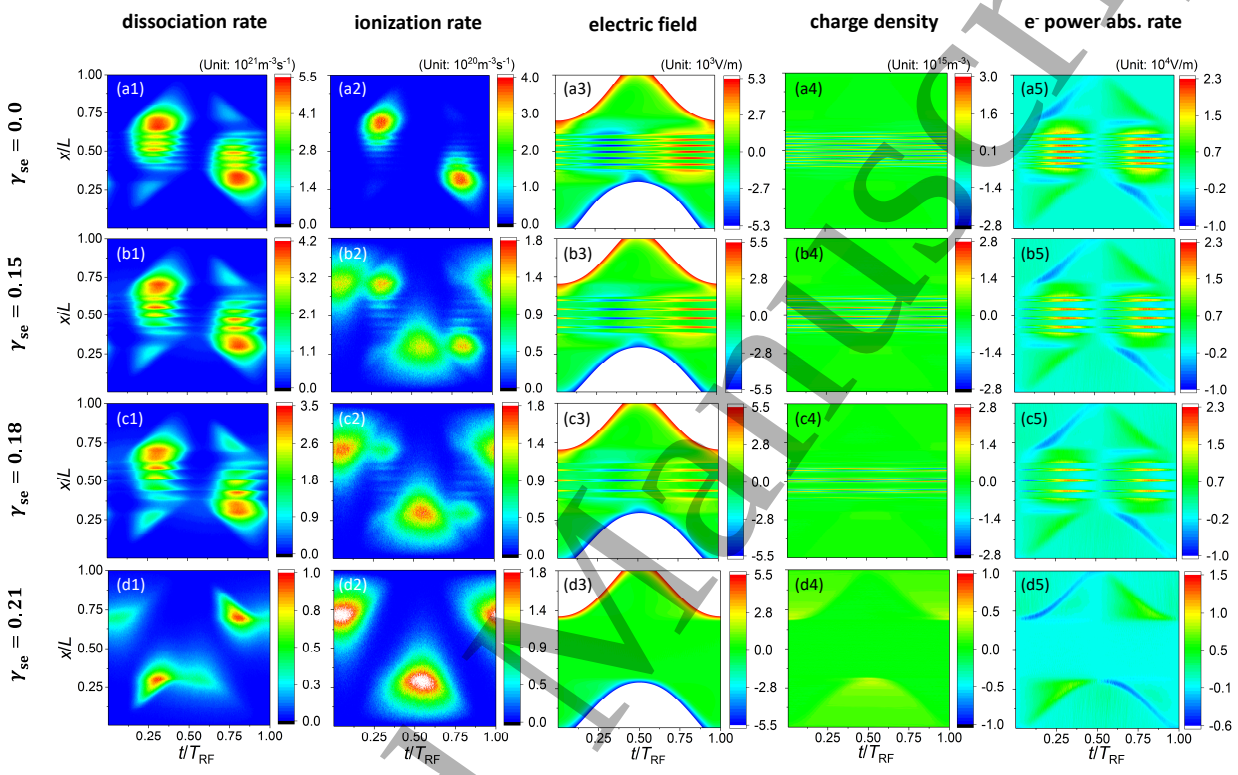

FIG. 3: The spatio-temporal plots of the electron-impact dissociation rate (first column), electron-impact ionization rate (second column), electric field (third column), net charge density (fourth column), and electron power absorption rate (fifth column) at different secondary electron emission coefficients. The conditions are the same as in figure 1.

Corresponding to the changes of ion density in figure 1, the striation gaps in the profiles of the electron-impact dissociative rate, ionization rate, electric field, charge density, and electron power absorption rate are enlarged with the enhanced secondary electron emission, and the striations finally disappear in the fourth row of figure 3, as the secondary emission coefficient is set to 0.21. More significantly, the ionization rate profiles show a transition of the operation mode with the increasing secondary emission coefficient. It is found in figure 3(a2) that when $\gamma_{se} = 0.0$, due to the electron heating by the striated bulk field, ionization occurs inside the plasma bulk and the ionization rate shows striated structure,

Accepted Manuscript

i.e., the operation is under STR mode. However, with enhancing the secondary electron emission, ionization in the bulk is weakened (figure 3(b2)-(d2)), whereas the ionization inside the sheaths is enhanced, meaning that, the γ-mode gradually becomes more important. Especially when the emission coefficient is large enough, such as $\gamma_{se} = 0.21$, the STR mode disappears and the γ-mode is greatly enhanced, indicating that the existence of the secondary electron emission induces the heating mode transition from STR mode to γ-mode.

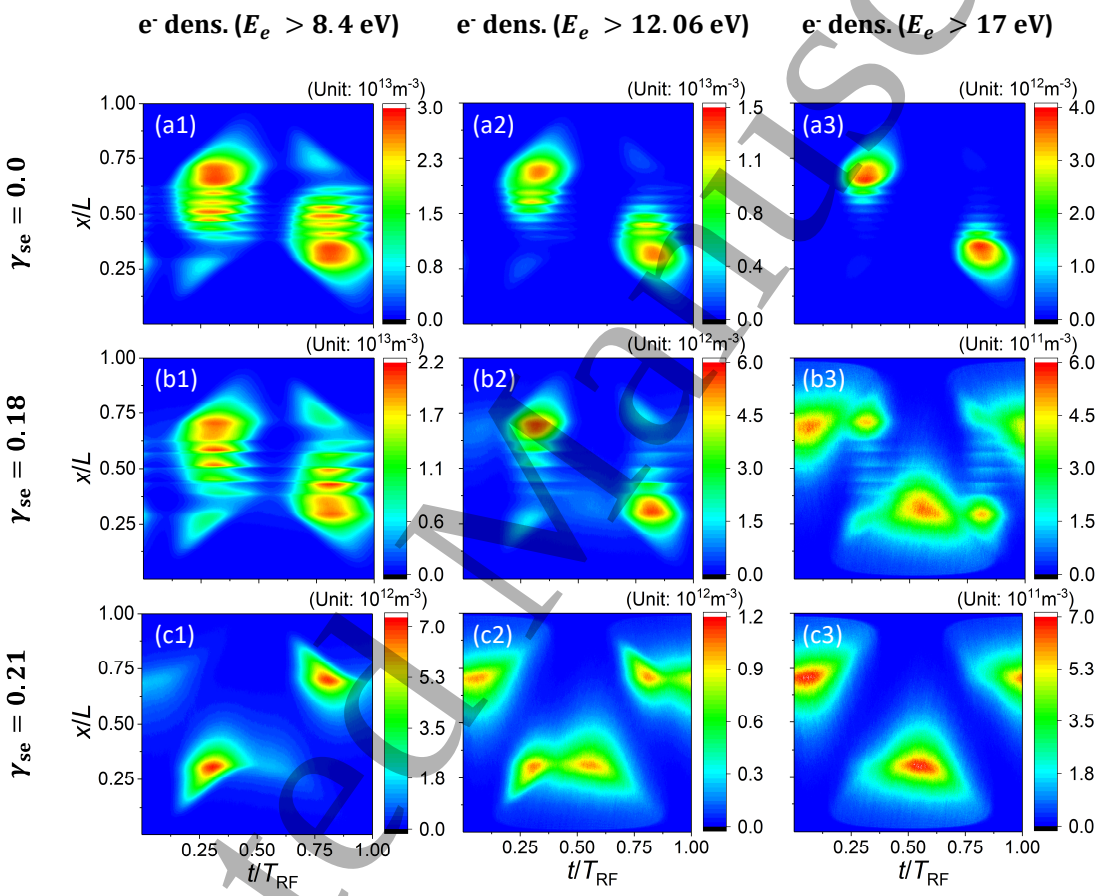

FIG. 4: The spatio-temporal plots of electron density with energy greater than 8.4 eV (first column), 12.06 eV (second column), and 17 eV (third column) at $\gamma_{se} = 0.0$, $\gamma_{se} = 0.18$, and $\gamma_{se} = 0.21$. The conditions are the same as in figure 1.

We also note that, different from the dissociation rate, the ionization rate in the bulk region is much weaker and the striated structure is not that evident, since its relatively high threshold value. In figure 4(a1) and (b1), we show the spatio-temporal distribution of the electron density, with the electron's kinetic energy larger than 8.4 eV (the threshold value of dissociation, reaction 12 in table 1), as the secondary emission coefficient $\gamma_{se} = 0$ and

Accepted Manuscript

$\gamma_{se} = 0.18$. It could be observed that lots of electrons in the bulk could reach 8.4 eV and be involved in the dissociation collision after being sufficiently accelerated in the electric field. However, the threshold value of ionization is 12.06 eV, which is too high for most of the bulk electrons to reach, as shown in figure 4(a2) and (b2). Indeed, the electrons are gradually accelerated by the bulk electric field. Within the first half of the RF period, the electrons move from the powered electrode to the grounded electrode, opposite to the direction of electric field, and continuously gain energy until collide with neutrals or reach the boundary of the collapse sheath. Most energetic electrons are near the grounded electrode in the first half period and near the powered electrode in the second half period. As a result, only the electrons approaching the collapse sheaths, which are in a small number, can reach the ionization threshold after being accelerated by the bulk field. For higher energies, such as 17 eV, fewer electrons in the bulk could reach, as shown in figure 4(a3) and (b3). Therefore, the ionization in the bulk is weaker than the dissociation, which could be observed over almost the whole bulk region.

Moreover, figure 4(b2) indicates that at $\gamma_{se} = 0.18$, the density of the electrons in the bulk with energy above the ionization threshold, is much larger than that in the sheaths. However, figure 3(c2) shows a higher ionization rate in the sheaths than the bulk region. This is caused by the significant acceleration of the secondary electrons in the sheaths and the rapid increase of the ionization cross section as the electron energy grows. According to Ref. [51], by which the ionization cross section adopted, we can observe a sharp growth in the ionization cross section as the electron energy exceeds the threshold energy, i.e., the ionization rate would increase rapidly with the electron energy. In figure 4(b3), we show the density of electrons with energy above 17 eV, from which we can see that high energy electrons in the sheaths are much more than that in the bulk. As a result, the electrons in the sheaths contribute more ionization to the discharge. Besides, the electron density distribution at $\gamma_{se} = 0.21$, with energy higher than the dissociation threshold is shown in figure 4(c1). It is seen that, different from figure 4(a1) and (b1), the electrons are mainly accelerated by the expanding sheaths under this condition and few electrons could be observed near the collapse sheaths due to the weakened bulk electric field. The electron density with the energy higher than 12.06 eV and 17 eV are shown in figure 4(c2) and (c3), in which, the secondary electrons are pronounced, leading to a contributive γ-mode in the discharge.

Accepted Manuscript

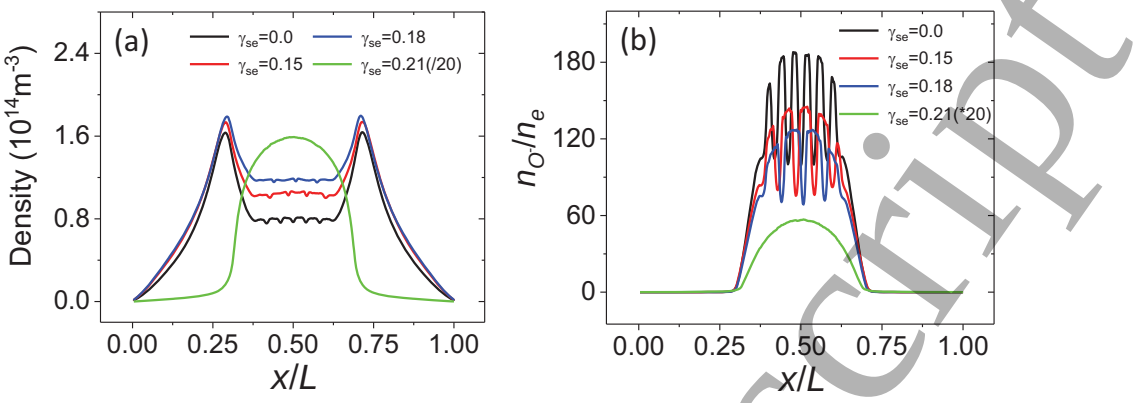

FIG. 5: Axial profiles of the time-averaged electron density (a) and electronegativity (b) at different secondary electron emission coefficients. The electron density is divided by a factor of 20 and the electronegativity is multiplied by 20 at $\gamma_{se} = 0.21$. The conditions are the same as in figure 1.

In order to further understand the breakdown of the striations induced by secondary electrons, figure 5(a) shows the emission coefficient dependence of the spatial distribution of time-averaged electron density. One could see that the electron density in the bulk increases with the secondary electron emission coefficient, and finally becomes a parabolic distribution. Figure 5(b) further shows the corresponding axial electronegativity, which decreases as γ_{se} varies from 0 to 0.21. Indeed, accounting for the increased conductivity with the growth number of electrons as γ_{se} increases, it is difficult to establish a striated electric field in the bulk, leading to weakened acceleration of electrons. As a result, the ionization becomes inadequate to compensate for the ion loss at the positions where the maximum ion density values need to be established. To obtain enough energy and ionization with neutral particles, electrons have to cross the electric field over a longer distance, leading to an increased striation gap to establish a new balance, at which the ion production equals to the loss. Ultimately, the changes of the electron density and electronegativity caused by the increase of γ_{se} give rise to the gradual increasing striation gap. As γ_{se} is large enough, the electronegativity becomes small enough, with the electric field weakened here. Thus, the electrons are hardly accelerated to the ionization threshold in the bulk and the striations disappear.

In addition, from figure 5(b), we can see that when γ_{se} is set from 0.0 to 0.18, the electronegativity is in the range of 120-190 at the positions of the maximum ion density, which is much higher than that in the common conditions. This is mainly caused by the

Accepted Manuscript

special characteristic of the "comb-like" profiles of ion density, and the much lower electron density near the discharge center. When the ion density is in "comb-like"distribution, the O^- density at the peaks is much higher than the density at the valleys, which also leads to a high electronegativity at the density peaks. Similar results could be found in [22], where the electronegativity at the positions of density peaks is in the range of $75 - 250$, much higher than the electronegativity at the density valleys with a value between 10 and 75. Indeed, although the electronegativity near the discharge center in figure 5(b) is high, the time and space averaged electronegativity is much lower and has a value between 41.9 and 49.3 for different secondary electron emission coefficients, which is similar to the results of Derzsi et al [56] for the conditions of single frequency discharges. It should also be noted that, the electrode gap and driving frequency in our simulation is relatively small, which is another possible reason for the high electronegativity. Similarly, a high electronegtivity was recently observed in oxygen discharges, and found to decrease with the increasing electrode gap [58] and operational frequency [59].

3.2 Influences of driving voltage and gas pressure on the operation mode transition

Fixing the driving frequency at 6 MHz, gas pressure at 40 Pa, and secondary emission coefficient at 0.15, we show the voltage effects in figure 6, in which the spatio-temporal electron-impact dissociation rate (first column), electron-impact ionization rate (second column), electric field (third column), net charge density (fourth column) and electron power absorption rate (fifth column) corresponding to different voltage amplitudes are given. In order to capture the gradual evolution process of two modes transition, i.e., from γ-mode to STR mode, a range of voltage amplitude from 150 V to 225 V is adopted. We can see that, the ionization rate in the bulk region is a little weakened when the voltage increases from 150 V to 200 V, and rapidly becomes almost invisible at 225 V, whereas the ionization near the sheath edges due to secondary electron emission becomes enhanced both in scope and intensity as the voltage increases. As we expect, the γ-mode gradually turns to be the main electron heating mode compared with the STR mode in sustaining the discharge with increasing the RF voltage. Moreover, along with this transition, the striation structure also shows a disruption as the voltage increases to 225 V. Figure 7(a) shows the O_2^+ density at the voltage amplitudes corresponding to figure 6. We can see that, when the voltage is

Accepted Manuscript

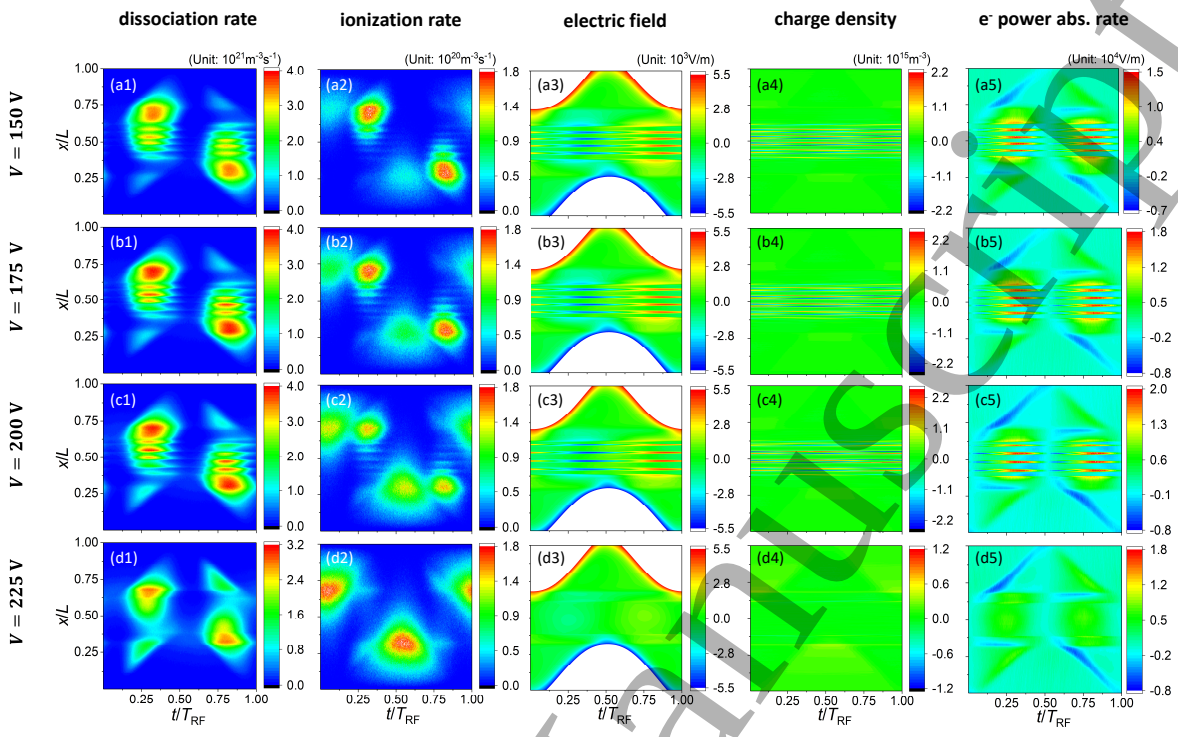

FIG. 6: The spatio-temporal plots of the electron-impact dissociation rate (first column), electron-impact ionization rate (second column), electric field (third column), net charge density (fourth column), and electron power absorption rate (fifth column) at different voltage amplitudes. The discharge parameters are: driving frequency $f = 6$ MHz, secondary emission coefficient $\gamma_{se} = 0.15$, and gas pressure $P = 40$ Pa.

less than 200 V, for the reason of the critical ion density for striations [22], the minimum densities of O_2^+ are comparable in the bulk. Whereas the maximum density increases with the voltage amplitude, giving rise to the enhancement of the ion flux on the electrode. As shown in figure 7(b), the time averaged positive ion flux on the powered electrode is increased as a function of the voltage amplitude, inducing definitely more intensive secondary electron emission and multiplication of the electrons in the sheaths, as the main reason for the heating mode transition. Another factor that should not be ignored for the enhancement of the γ-mode and the heating mode transition is the enhancement of the secondary electron acceleration in the sheaths. At high voltages, the secondary electrons get more energy in the sheaths, which makes the ionization more intense. As a result, ionization caused by secondary electrons is more pronounced and γ-mode becomes the main heating mode in the discharge at high voltage amplitudes.

Accepted Manuscript

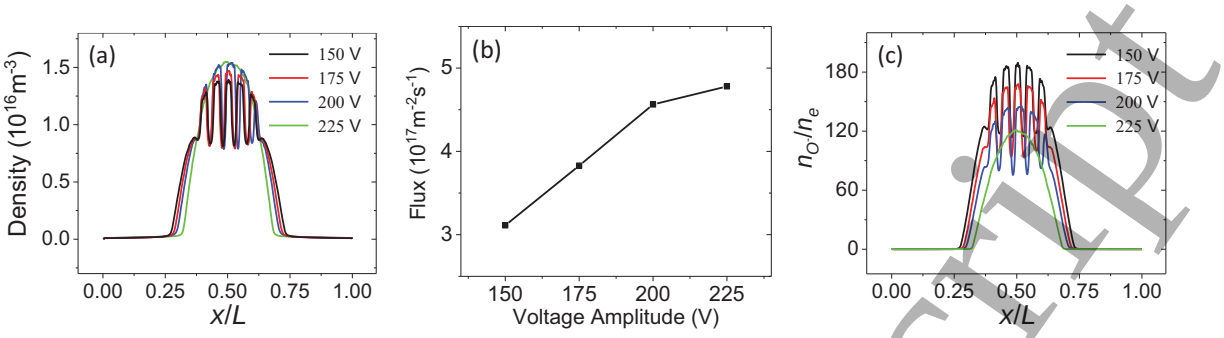

FIG. 7: Time-averaged profiles of the axial O_2^+ ion densities (a), O_2^+ ion flux on the powered electrode as a function of the voltage amplitude (b), and the axial electronegativity at different voltage amplitudes (c). The conditions are the same as in figure 6.

From the ion-ion model [22], the resonance condition is the ion density $n_{\rm i} > n_{\rm critical} = \varpi_{\rm rf}^2 \varepsilon_0 \mu / e^2$, where e is the elementary charge, $\varpi_{\rm rf}$ is the driving angular frequency, ε_0 is the permittivity in vacuum and μ is the reduced mass of the positive and negative ions. As the driving frequency is set to 6 MHz here, the critical density is about 0.87×10^{16} m^{-3}. It is seen that, when the voltage amplitude is set to 225 V, the ion density still meets this condition, but the striations disappear. The disruption of the striations is induced by the increase of the electron density and consequently the decrease of electronegativity, which is neglected in the ion-ion model for simplification. Figure 7(c) shows the time averaged electronegativity over the discharge space. It is seen that the electronegativity gradually decreases from 180 at 150V to 140 at 200 V, and further drops to 120 at the discharge center when the voltage increases to 225 V. The decreased electronegativity leads to a slight increase of the striation gap when the voltage is less than 200 V, as shown in figure 7(a). In the case of 225 V, the electric field in the bulk region is too weak to accelerate the electrons to exceed the ionization threshold. It can be seen in figure 6(d1) and (d2) that the ionization in the bulk is quit weak compared with the dissociation rate. Thus, the striations could not be maintained in the bulk region. Meanwhile, the ionization caused by the secondary electrons is strong enough to sustain the discharge. Therefore, the heating mode transition occurs. In addition, when a higher voltage amplitude is set, a much lower electronegativity, which makes the discharge be weak electronegative, is also observed in our investigation.

Furthermore, we also investigate the influence of the gas pressure in figure 8, in which the driving frequency $f = 6$ MHz, voltage amplitude $V = 200$ V, and secondary emission coefficient $\gamma_{\rm se} = 0.15$ are fixed, and the spatio-temporal electron-impact dissociation rate

Accepted Manuscript

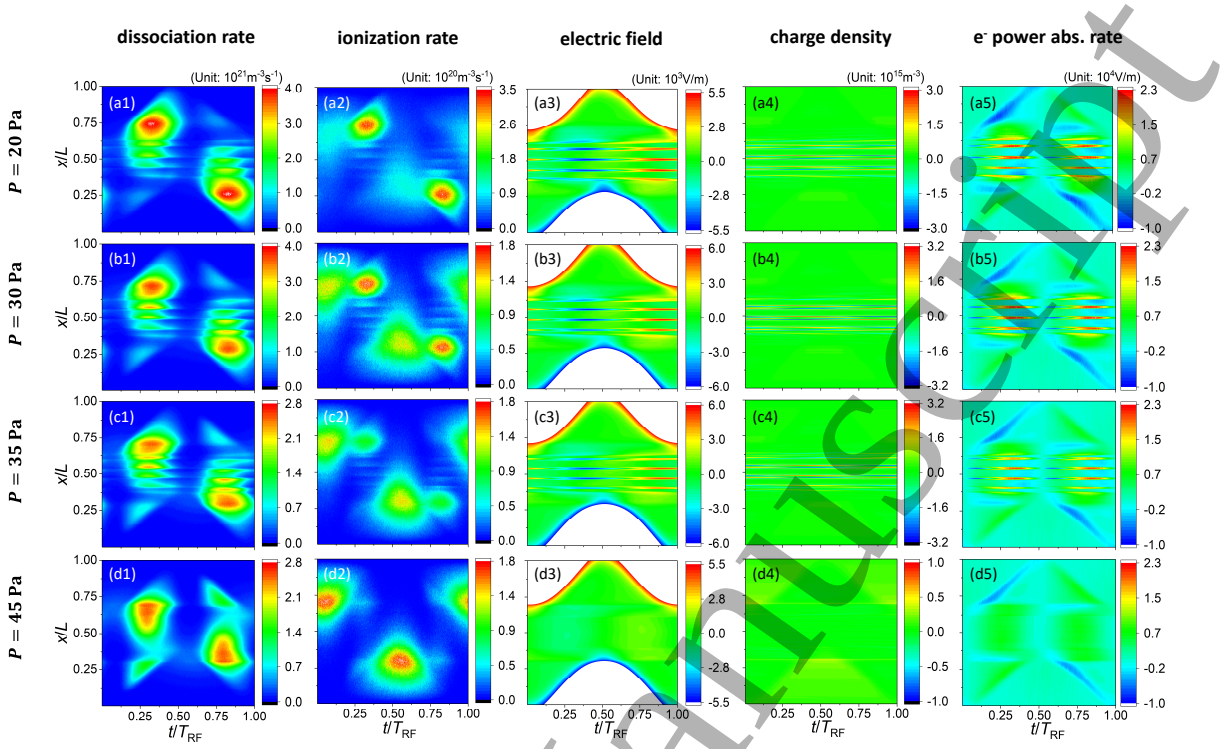

FIG. 8: The spatio-temporal plots of the electron-impact dissociation rate (first column), electron-impact ionization rate (second column), electric field (third column), net charge density (fourth column), and electron power absorption rate (fifth column) at different gas pressures. The discharge parameters are: driving frequency $f = 6$ MHz, secondary emission coefficient $\gamma_{se} = 0.18$, and voltage amplitude $V = 200$ V.

(first column), electron-impact ionization rate (second column), electric field (third column), net charge density (fourth column) and electron power absorption rate (fifth column) at different gas pressures (20 - 45 Pa) are shown. It is seen that the maximum ionization rate caused by secondary electrons is slightly increased as the pressure increases. However, the maximum ionization induced by the STR mode near the collapse sheaths becomes weakened when the gas pressure increases. Therefore, the γ-mode gradually starts to play a more effective role in the discharge compared with the STR mode, which also leads to the final striation disruption as the gas pressure is set to 45 Pa. The weakening of STR mode is mainly caused by insufficient heating of electrons in the bulk region at higher pressures. In this case, the collisions with relatively low energy thresholds are more frequent. For instance, in figure 9(a), the time averaged electron-impact excitation rate increases in the bulk with the increasing gas pressure, revealing that more electrons consume their energy

Accepted Manuscript

by the excitation process with the threshold energy about 4.5 eV. As a result, although lots of electrons could reach collapsing the sheath edges, only a small proportion of them could achieve the ionization threshold. As shown in figure 9(b), the time-averaged ionization rate decreases rapidly. This weakening of STR mode caused by the increasing gas pressure, makes the γ-mode play an increasingly important role in the discharge.

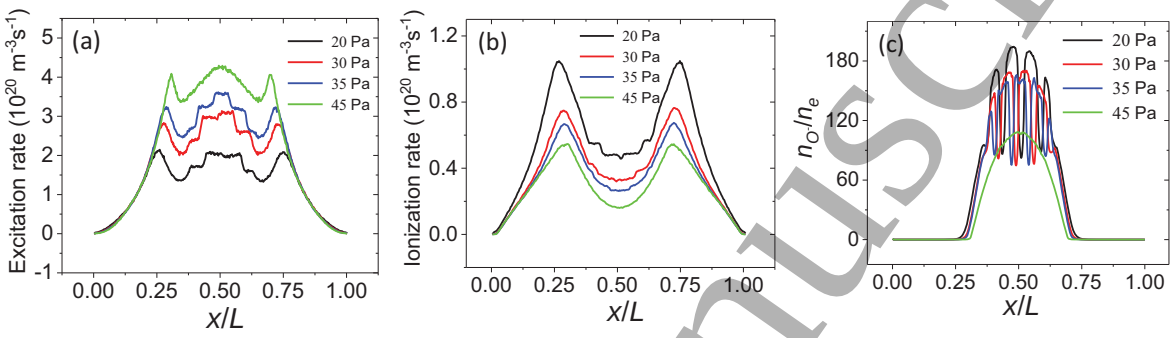

FIG. 9: Axial profiles of the time-averaged electron-impact excitation rate (a), electron-impact ionization rate (b), and electronegativity (c) at different gas pressure. The conditions are the same as in figure 8.

In addition, figure 9(c) shows the time averaged electronegativity at different gas pressures. It is found that the electronegativity is decreased as the gas pressure increases. This relationship between the electronegativity and gas pressure is consistent with the simulations of Gudmundsson et al [60], in which, the gas pressure dependence of the discharge properties in a capacitively coupled oxygen discharge was explored, with the electrode gap of 4.5 cm and the pressure range of 1.3 - 66.7 Pa adopted. They found that the electronegativity decreases with the increasing discharge pressure, and concluded that this result is greatly related to the significant influence of the detachment by metastable singlet molecule $O_2(a^1\Delta_g)$ on electron heating processes. However, in our work, although the decreased electronegativity would lead to an increased striation gap, the average striation gap in figure 8 is slightly decreased as the pressure increases to 35 Pa. The similar results could be found in CF_4 discharges [21], which is considered to be induced by the increasing collision frequency. According to reference [22], the amplitude of the relative displacement of the positive and negative ions is inversely proportional to the collision frequency. Thus, under the joint influence of the changes in electronegativity and collision frequency, the striation gap is not enlarged as expected. But as the pressure is set to 45 Pa, the electronegativity in the bulk is low enough, finally resulting in the disruption of the striations.

Accepted Manuscript

4. CONCLUSION AND DISCUSSION

Using a 1D3V PIC/MCC model, we investigate the secondary electron effects on the striation structures and electron heating mode transitions in oxygen discharges. It is obvious that lower electron density and higher electronegativity are necessary for the existence of the striations. Under the parameters applied in the simulations, "comb-like" profiles of ion densities are established when the secondary electron emission is not strong enough. In this case, in all the profiles of dissociation rate, electric field, net charge density, and electron power absorption rate, striation structures are observed.

More significantly, as the increase of γ_{se}, the striation gaps are enlarged and the striation number decreases. Especially when $\gamma_{\mathrm{se}} = 0.21$, the striations disrupt completely. When γ_{se} increases, ionization caused by the secondary electrons are more remarkable and the increasing electron density enhances the conductivity in the plasma bulk, which leads to an reduced bulk electric field. As a result, the electrons can hardly obtain enough energy in the bulk and the ionization collisions are inadequate to balance the consumption of the ions at the positions of the ion density peaks. Thus, an electric field, which covers a longer distance, is needed for electrons to get more energy and establish a new balance. Consequently, the enhancement of the secondary electron emission leads to the increasing striation gap and further the striation disruption.

In our investigation, we further investigate the electron heating mode transition with the involvement of the secondary electron emission. When γ_{se} increases, ionization caused by the bulk electrons becomes weakened due to insufficient electron acceleration in the bulk electric field, leading to the weakened STR mode. Meanwhile, the appearance of large numbers of secondary electrons enhances the γ-mode. As a result, the γ-mode gradually becomes comparable to the STR mode, and even possibly dominate the discharge when the electron emission coefficient is large enough.

Furthermore, the influences of driving voltage and gas pressure on the operation mode transition induced by secondary electrons are also discussed. When a fixed γ_{se} is set, γ-mode is found to be more important compared to STR mode in the discharge either by increasing the voltage amplitude or the gas pressure, but owing to completely different mechanisms. When the voltage amplitude increases, the increasing ion density and ion flux lead to more secondary electrons, which, after being accelerated in the sheaths, would ionize with neutral

Accepted Manuscript

particles and make the γ-mode enhanced. In contrast, at higher gas pressures, the collisions with low energy thresholds become more frequent and consume more electron energy in the bulk, resulting in fewer electrons with enough ionization energy near the sheath edge. As a result, the increasing pressure makes the γ-mode more contributive to the discharge.

In this work, we primarily discuss the effects of secondary electron emission on the striation structure and the electron heating mode transition in electronegative oxygen. By further performing the PIC simulations and adjusting the $O_2(a^1\Delta_g)$ wall quenching coefficient, changes of the striation structure are observed (not shown here). A detailed investigation is expected to be carried out in the future.

Acknowledgements

This work was supported by the National Natural Science Foundation of China (Grant No. 11675036, 11275038 and 11405019).

[1] Lieberman M A and Lichtenberg A J 2005 *Principles of Plasma Discharges and Materials Processing* 2nd edn (Wiley-Interscience)

[2] Chabert P and Braithwaite N 2011 *Physics of Radio-Frequency Plasmas* (Cambridge University Press)

[3] Makabe T and Petrović Z 2006 *Plasma Electronics : Applications in Microelectronic Device Fabrication* (Taylor & Francis)

[4] Kullig C, Wegner T and Meichsner J 2015 Instabilities in a capacitively coupled oxygen plasma *Phys. Plasmas* **22** 043515

[5] Lichtenberg A J, Kouznetsov I G, Lee Y T, Lieberman M A, Kaganovich I D and Tsendin L D 1997 Modelling plasma discharges at high electronegativity *Plasma Sources Sci. Technol.* **6** 437

[6] Booth J P, Cunge G, Chabert P and Sadeghi N 1999 CFx radical production and loss in a CF4 reactive ion etching plasma: Fluorine rich conditions *J. Appl. Phys.* **85** 3097

[7] Bruneau B, Korolov I, Lafleur T, Gans T, O'Connell D, Greb A, Derzsi A, Donko Z, Brandt S, Schungel E, Schulze J, Johnson E and Booth J P 2016 Slope and amplitude asymmetry effects on low frequency capacitively coupled carbon tetrafluoride plasmas *J. Appl. Phys.* **119** 163301

Accepted Manuscript

[8] Lieberman M A and Godyak V A 1998 From Fermi acceleration to collisionless discharge heating *IEEE Trans. Plasma Sci.* **26** 955

[9] Liu Y X, Zhang Q Z, Jiang W, Hou L J, Jiang X Z, Lu W Q and Wang Y N 2011 Collisionless bounce resonance heating in dual-frequency capacitively coupled plasmas *Phys. Rev. Lett.* 107 055002

[10] Lafleur T and Booth J P 2012 Control of the ion flux and ion energy in CCP discharges using non-sinusoidal voltage waveforms *J. Phys. D: Appl. Phys.* **45** 395203

[11] Schulze J, Derzsi A, Dittmann K, Hemke T, Meichsner J and Donko Z 2011 Ionization by Drift and ambipolar electric fields in electronegative capacitive radio frequency plasmas *Phys. Rev. Lett.* **107** 275001

[12] Derzsi A, Schungel E, Donko Z and Schulze J 2015 Electron heating modes and frequency coupling effects in dual-frequency capacitive CF4 plasmas *Open Chem* **13** 346

[13] Liu G H, Liu Y X, Wen D Q and Wang Y N 2015 Heating mode transition in capacitively coupled CF4 discharges: comparison of experiments with simulations *Plasma Sources Sci. Technol.* **24** 034006

[14] Schulze J, Heil B G, Luggenholscher D, Mussenbrock T, Brinkmann R P and Czarnetzki U 2008 Electron beams in asymmetric capacitively coupled radio frequency discharges at low pressures *J. Phys. D: Appl. Phys.* **41** 042003

[15] Surendra M and Graves D B 1991 Electron acoustic-waves in capacitively coupled low-pressure rf glow-discharges *Phys. Rev. Lett.* **66** 1469

[16] Dittmann K, Matyash K, Nemschokmichal S, Meichsner J and Schneider R 2010 Excitation mechanisms and sheath dynamics in capacitively coupled radio-frequency oxygen plasmas contrib. *Plasm. Phys.* **50** 942

[17] Gozadinos G, Turner M M and Vender D 2001 Collisionless electron heating by capacitive rf sheaths *Phys. Rev. Lett.* **87** 135004

[18] Jiang W, Xu X, Dai Z L and Wang Y N 2008 Heating mechanisms and particle flow balancing of capacitively coupled plasmas driven by combined dc/rf sources *Phys. Plasmas* **15** 033502

[19] Godyak V A and Khanneh A S 1986 Ion-Bombardment Secondary-electron maintenance of steady rf discharge *IEEE Trans. Plasma Sci.* **14** 112

[20] Liu Y X, Schungel E, Korolov I, Donko Z, Wang Y N and Schulze J 2016 Experimental observation and computational analysis of striations in electronegative capacitively coupled

Accepted Manuscript

radio-frequency plasmas *Phys. Rev. Lett.* **116** 255002

[21] Liu Y X, Korolov I, Schungel E, Wang Y N, Donko Z and Schulze J 2017 Striations in electronegative capacitively coupled radio-frequency plasmas: Effects of the pressure, voltage, and electrode gap *Phys. Plasmas* **24** 073512

[22] Liu Y X, Korolov I, Schungel E, Wang Y N, Donko Z and Schulze J 2017 Striations in electronegative capacitively coupled radio-frequency plasmas: analysis of the pattern formation and the effect of the driving frequency *Plasma Sources Sci. Technol.* **26** 055024

[23] Zhang Q Z, Wang Y N and Bogaerts A 2014 Heating mode transition in a hybrid direct current/dual-frequency capacitively coupled CF4 discharge *J. Appl. Phys.* **115** 223302

[24] Donko Z, Schulze J, Czarnetzki U, Derzsi A, Hartmann P, Korolov I and Schungel E 2012 Fundamental investigations of capacitive radio frequency plasmas: simulations and experiments *Plasma Phys. Control. Fusion* **54** 124003

[25] Liu Y X, Zhang Q Z, Liu J, Song Y H, Bogaerts A and Wang Y N 2013 Electron bounce resonance heating in dual-frequency capacitively coupled oxygen discharges *Plasma Sources Sci. Technol.* **22** 025012

[26] Liu Y X, Zhang Q Z, Liu J, Song Y H, Bogaerts A and Wang Y N 2012 Effect of bulk electric field reversal on the bounce resonance heating in dual-frequency capacitively coupled electronegative plasmas *Appl. Phys. Lett.* **101** 114101

[27] Belenguer P and Boeuf J P 1990 Transition between different regimes of rf glow-discharges *Phys. Rev. A* **41** 4447

[28] Brandt S, Berger B, Schungel E, Korolov I, Derzsi A, Bruneau B, Johnson E, Lafleur T, O'Connell D, Koepke M, Gans T, Booth J P, Donko Z, and Schulze J 2016 Electron power absorption dynamics in capacitive radio frequency discharges driven by tailored voltage waveforms in CF4 *Plasma Sources Sci. Technol.* **25** 045015

[29] Schulze J, Donko Z, Schungel E and Czarnetzki U 2011 Secondary electrons in dual-frequency capacitive radio frequency discharges *Plasma Sources Sci. Technol.* **20** 045007

[30] Derzsi A, Donko Z and Schulze J 2013 Coupling effects of driving frequencies on the electron heating in electronegative capacitive dual-frequency plasmas *J. Phys. D: Appl. Phys.* **46** 482001

[31] Proshina O V, Rakhimova T V, Rakhimov A T and Voloshin D G 2010 Two modes of capacitively coupled rf discharge in CF4 *Plasma Sources Sci. Technol.* **19** 065013

Accepted Manuscript

[32] Schulze J, Donko Z, Derzsi A, Korolov I and Schuengel E 2015 The effect of ambipolar electric fields on the electron heating in capacitive RF plasmas *Plasma Sources Sci. Technol.* **24** 015019

[33] Schulze J, Donko Z, Heil B G, Luggenholscher D, Mussenbrock T, Brinkmann R P and Czarnetzki U 2008 Electric field reversals in the sheath region of capacitively coupled radio frequency discharges at different pressures *J. Phys. D: Appl. Phys.* **41** 105214

[34] Godyak V A, Piejak R B and Alexandrovich B M 1992 Evolution of the electron-energy-distribution function during rf discharge transition to the high-voltage mode *Phys. Rev. Lett.* **68** 40

[35] Denpoh K and Nanbu K 1998 Self-consistent particle simulation of radio-frequency CF4 discharge with implementation of all ion-neutral reactive collisions *J. Vac. Sci. Technol. A* **16** 1201

[36] Denpoh K and Nanbu K 2000 Self-consistent particle simulation of radio frequency CF4 discharge: Effect of gas pressure *Japanese J. Appl. Phys.* **39** 2804

[37] Yin Z F, Sun L, Zou H L and Cheng E 2015 Two dimensional PMMA nanofluidic device fabricated by hot embossing and oxygen plasma assisted thermal bonding methods *Nanotechnology* **26** 215302

[38] Ham S W, Hong H P, Kim J W, Kim J H, Kim K B, Park C W and Min N K 2015 Comparison of Gas Sensors Based on Oxygen Plasma-Treated Carbon Nanotube Network Films with Different Semiconducting Contents *J Electron Mater* **44** 1344

[39] Greb A, Niemi K, O'Connell D and Gans T 2013 The influence of surface properties on the plasma dynamics in radio-frequency driven oxygen plasmas: Measurements and simulations *Appl. Phys. Lett.* **103** 244101

[40] Katsch H M, Sturm T, Quandt E and Dobele H F 2000 Negative ions and the role of metastable molecules in a capacitively coupled radiofrequency excited discharge in oxygen *Plasma Sources Sci. Technol.* **9** 323

[41] Greb A, Gibson A R, Niemi K, O'Connell D and Gans T 2015 Influence of surface conditions on plasma dynamics and electron heating in a radio-frequency driven capacitively coupled oxygen plasma *Plasma Sources Sci. Technol.* **24** 044003

[42] Gibson A R and Gans T 2017 Controlling plasma properties under differing degrees of electronegativity using odd harmonic dual frequency excitation *Plasma Sources Sci. Technol.* **26** 115007

Accepted Manuscript

[43] Bronold F X, Matyash K, Tskhakaya D, Schneider R and Fehske H 2007 Radio-frequency discharges in oxygen: I. Particle-based modelling *J. Phys. D: Appl. Phys.* **40** 6583

[44] Derzsi A, Lafleur T, Booth J P, Korolov I and Donko Z 2016 Experimental and simulation study of a capacitively coupled oxygen discharge driven by tailored voltage waveforms *Plasma Sources Sci. Technol.* **25** 015004

[45] Gudmundsson J T and Lieberman M A 2015 On the role of metastables in capacitively coupled oxygen discharges *Plasma Sources Sci. Technol.* **24** 035016

[46] Gudmundsson J T, Kouznetsov I G, Patel K K and Lieberman M A 2001 Electronegativity of low-pressure high-density oxygen discharges *J. Phys. D: Appl. Phys.* **34** 1100

[47] Zhang Q Z, Jiang W, Hou L J and Wang Y N 2011 Numerical simulations of electrical asymmetry effect on electronegative plasmas in capacitively coupled rf discharge *J. Appl. Phys.* **109** 013308

[48] Schungel E, Zhang Q Z, Iwashita S, Schulze J, Hou L J, Wang Y N and Czarnetzki U 2011 Control of plasma properties in capacitively coupled oxygen discharges via the electrical asymmetry effect *J. Phys. D: Appl. Phys.* **44** 285205

[49] Gudmundsson J T and Snorrason D I 2017 On electron heating in a low pressure capacitively coupled oxygen discharge *J. Appl. Phys.* **122** 193302

[50] Vahedi V and Surendra M 1995 A monte-carlo collision model for the particle-in-cell method - applications to argon and oxygen discharges *Comput. Phys. Commun.* **87** 179

[51] Gudmundsson J T, Kawamura E and Lieberman M A 2013 A benchmark study of a capacitively coupled oxygen discharge of the oopd1 particle-in-cell Monte Carlo code *Plasma Sources Sci. Technol.* **22** 035011

[52] Proto A and Gudmundsson J T 2018 The role of surface quenching of the singlet delta molecule in a capacitively coupled oxygen discharge *Plasma Sources Sci. Technol.* **27** 074002

[53] Sharpless R L, Jusinski L E and Slanger T G 1989 Surface-Chemistry Of Metastable Oxygen .1. Production And Loss Of the 4-5 Ev States *J. Chem. Phys.* **91** 7936

[54] Sharpless R L and Slanger T G 1989 Surface-Chemistry Of Metastable Oxygen .2. Destruction Of O-2(A1-Delta-G) *J. Chem. Phys.* **91** 7947

[55] Crannage R P, Dorko E A, Johnson D E and Whitefield P D 1993 Surface Deactivation Efficiencies for O2(1-Delta)(G) on a Range Of Materials .1. Pyrex, Nickel, Copper, Nickel Copper Alloy And Inconel *Chem Phys* **169** 267

Accepted Manuscript

[56] Derzsi A, Bruneau B, Gibson A R, Johnson E, O'Connell D, Gans T, Booth J P and Donko Z 2017 Power coupling mode transitions induced by tailored voltage waveforms in capacitive oxygen discharges *Plasma Sources Sci. Technol.* **26** 034002

[57] Donko Z Derzsi A Vass M Schulze J Schuengel E and Hamaguchi S 2018 Ion energy and angular distributions in low-pressure capacitive oxygen RF discharges driven by tailored voltage waveforms *Plasma Sources Sci. Technol.* **27** 104008

[58] You K H, Schulze J, Derzsi A, Donko Z, Yeom H J, Kim J H, Seong D J and Lee Hyo-Chang 2019 Experimental and computational investigation of the effect of the electrode gap on capacitively coupled radio frequency oxygen discharges *Phys. Plasmas* **26** 013503

[59] Gudmundsson J T, Snorrason D I and Hannesdottir H 2018 The frequency dependence of the discharge properties in a capacitively coupled oxygen discharge *Plasma Source Sci. Technol.* **27** 025009

[60] Gudmundsson J T and Ventejou B 2015 The pressure dependence of the discharge properties in a capacitively coupled oxygen discharge *J. Appl. Phys.* **118** 153302

Accepted Manuscript